Todd G. Nelson[1]
Department of Engineering,
University of Southern Indiana,
Evansville, IN 47712
e-mail: tgnelson@usi.edu

Luis M. Baldelomar Pinto
Department of Engineering,
University of Southern Indiana,
Evansville, IN 47712
e-mail: lmbaldelom@eagles.usi.edu

Jared T. Bruton
Compliant Mechanisms Research Group,
Department of Mechanical Engineering,
Brigham Young University,
Provo, UT 84604
e-mail: jared.bruton@gmail.com

Zhicheng Deng
School of Aeronautic Science and Engineering,
Beijing University of Aeronautics & Astronautics,
Beijing 100191, China
e-mail: deng@buaa.edu.cn

Curtis G. Nelson
Department of Mathematics,
Brigham Young University—Idaho,
Rexburg, ID 83460
e-mail: nelsoncu@byui.edu

Larry L. Howell
Compliant Mechanisms Research Group,
Department of Mechanical Engineering,
Brigham Young University,
Provo, UT 84604
e-mail: lhowell@byu.edu

Deployable Convex Generalized Cylindrical Surfaces Using Torsional Joints

The ability to deploy a planar surface to a desired convex profile with a simple actuation can enhance foldable or morphing airfoils, deployable antennae and reflectors, and other applications where a specific profile geometry is desired from a planar sheet. A model using a system of rigid links joined by torsional springs of tailorable stiffness is employed to create an approximate curved surface when two opposing tip loads are applied. A system of equations describing the shape of the surface during deployment is developed. The physical implementation of the model uses compliant torsion bars as the torsion springs. A multidimensional optimization algorithm is presented to place joints to minimize the error from the rigid-link approximation and account for additional manufacturing and stress considerations in the torsion bars. A proof is presented to show that equal torsion spring spacing along the horizontal axis of deployed parabolic profiles will result in minimizing the area between the model's rigid-link approximation and smooth curve. The model is demonstrated through the physical construction of a deployable airfoil surface and a metallic deployable parabolic reflector. [DOI: 10.1115/1.4049951]

Keywords: compliant mechanisms, folding and origami

1 Introduction

The objective of this research is to present a model which can be used to create a deployable surface with a simple actuation that closely approximates a generalized cylindrical surface, such as the one shown in Fig. 1, using torsional joints which can be manufactured as 2D geometries with thickness. The ability to transition from a flat sheet to a predetermined shape can lead to advances in applications such as stowable reflectors incorporated in space mechanisms, tunable optical devices, morphing aerodynamic or hydrodynamic structures, and conforming components like circuit boards to curved shapes. This research includes and expands on work presented at the Mechanisms and Robotics Conference at ASME IDETC 2020 [1].

A generalized cylindrical surface is one of the three classes of curved developable surfaces. A developable surface can be formed from a planar surface through bending without any stretching or tearing [2]. A generalized cylinder is formed by translating a straight line, called the generator line, along a path in a plane perpendicular to the generator line. The path is called the directrix of the generalized cylinder. For example, a circular directrix would give rise to the common right circular cylinder. The method presented in this research enables the design of deployable, approximate generalized cylindrical surfaces where the directrix is a convex curve that does not self-intersect. Furthermore, the determination of the joint placement is investigated through optimization techniques to minimize error in the approximation of the surface and to include constraints on various parameters to ensure the functionality and manufacturability of the surface.

Part of the modeling presented in this research includes the characterization of the stiffness of a deployable surface. While this

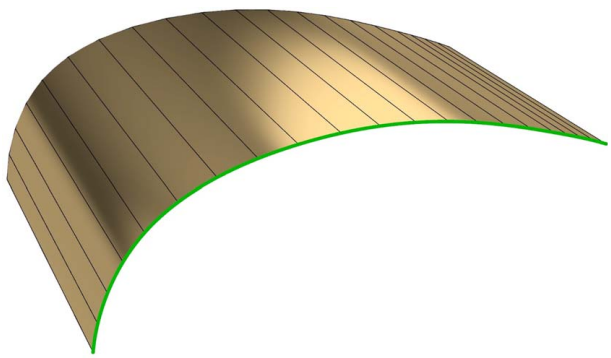

Fig. 1 A generalized cylinder with ruling lines (thin lines) and a convex directrix (thick edge)

[1]Corresponding author.

Contributed by the Mechanisms and Robotics Committee of ASME for publication in the Journal of Mechanisms and Robotics. Manuscript received September 25, 2020; final manuscript received January 14, 2021; published online March 12, 2021. Assoc. Editor: Leila Notash.

research focuses on using compliant torsional joints to introduce flexibility along straight lines in the surface (simulating the introduction of pin joints with a stiffness), there is a substantial body of work on modeling stiffness of structures and manipulators in more general configurations and with joints exhibiting more degrees-of-freedom. For example, work in characterizing the stiffness of manipulators and soft robotic arms has been approached through matrix structural analysis [3,4], finite element analysis [5,6], and the virtual joint method [7–9].

Surfaces which can be controlled or predictably changed offer advantages in situations where a change in occupied space or a dynamic response to an environment is desired [10]. Varying geometry of morphing elements can produce smooth curved surfaces [11], while other techniques achieve morphing through approximating curved surfaces with discrete morphing elements [12]. Morphing can also be used to provide locomotion as was accomplished with printing liquid crystal elastomer bilayers [13] or transition between stable states as was done with a compliant six-bar dwell mechanism [14].

Origami and origami-inspired mechanisms provide examples of surfaces where a change from one state, perhaps a tightly compacted state, to another state, a deployed state, is desired. Examples of these include bio-inspired wing structures [15], a diameter-changing origami wheel [16], and an origami-based heart stent [17]. Self-folding qualities can induce morphing with actuation methods such as thermally activated shape memory alloys [18]. Kirigami has also been leveraged to create morphing structures in response to temperature and light changes [19,20]. Origami and kirigami methods can enable simple manufacturing methods with complex morphing motions.

Morphing surfaces have also been used to enhance the performance through creating desirable geometries and profiles. Morphing wings and flight surfaces have been investigated to create structures which can be dynamically modified to achieve geometries which perform well under varying environments or conditions [21–25]. Deployable reflectors use the principle of morphing or changing surfaces to create the desired collection shape while still having the ability to stow compactly [26–30]. Optimization is commonly employed to assist in the determination of geometry for these types of morphing geometries [31,32].

This work specifically looks at generalized cylindrical surfaces, which are one of the four possible developable surfaces resulting from curved folds or creases in a surface [2]. The results of this work could possibly be incorporated into mechanisms and structures derived from curved-fold origami patterns to facilitate specific panel shapes or further increase the propensity of a panel to take a certain shape during deployment [33]. In comparison to the methods presented in the previous paragraph, the method presented here has characteristics of having an analytical model to create a geometry to approximate a deployed profile (as opposed to relying on finite element simulations or other numerical methods) and being simple to actuate through a single contractile element. Additionally, when torsion joints are used to form the flexible portions of the surface, the entire deployable surface can be made with planar-limited manufacturing techniques. The presentation of an optimization method to determine the placement of joint locations to minimize the error from approximating a continuous curved surface as a series of rigid links could be applied to several of the existing methods for creating morphing surfaces.

2 Method

2.1 Spring and Rigid-Link Model for Generalized Cylindrical Deployable Surfaces. A model for creating generalized cylindrical deployable surfaces uses a system of rigid links joined by torsional springs that is actuated from a flat state by opposing tip loads to form a desired directrix in a deployed state. The desired directrix is used to calculate the required stiffness of the torsional springs between each rigid link.

Let $L_1, L_2, \ldots, L_{N+1}$ be the lengths of $N+1$ rigid links in the system and N is the number of joints between the links. Let $k_1, k_2, \ldots, k_N$ denote the equivalent stiffness of the torsion springs between the rigid links as shown in Fig. 2(*a*). The rigid-link system can be placed in the desired curved shape, represented by the function $y_{\text{desired}}(x)$, where all of the endpoints of the rigid links lie upon the curve. The deployed link angles $\theta_0, \theta_1, \ldots, \theta_N$, the deployed heights $y_1, y_2, \ldots, y_N$, and the distance between the tip loads r as shown in Fig. 2(*b*) can be determined from geometry. This information can be found using vectors that represent each of the links to calculate the angle between these vectors to obtain the deployed link angles and using $y_{\text{desired}}(x)$ to find the deployed heights for each x corresponding to a joint location.

With the system of rigid links in the desired curved shape, the moment at the ith joint, M_i, for joints $i = 1$ to N can be expressed as

$$M_i = k_i \theta_i \tag{1}$$

The free-body diagram drawn for the ith joint in Fig. 3 with opposing tip loads, F, shows that the moment, M_i, can also be expressed as

$$M_i = F y_i \tag{2}$$

By equating Eqs. (1) and (2), we can find an expression for the stiffness of each torsion spring in terms of known geometry as

$$k_i = \frac{F y_i}{\theta_i} \tag{3}$$

The lamina emergent torsion (LET) is a compliant joint that allows for a twisting motion [34–36]. A full LET joint consists of four torsion bars, a set of two parallel torsion bars (also called a torsional parallel joint [37]) in series with another set of two parallel torsion bars. LET joints can be chained together to form lines of torsion bars [33,38]. The lines of parallel torsion bars can act as the torsion springs in the model. An example of the geometry of a LET joint chain with two torsion bars on each ruling line is detailed in Fig. 4. The torsion bars of the LET joints are well suited to the model for deployable surfaces as the joints can be planar manufactured as part of a sheet, have a relatively stable axis of rotation, and have geometry which can be modified to change the stiffness of the joint in a predictable way using spring models [34,39]. For example, the length, width, or thickness of the torsion bars can be changed to specify a certain stiffness.

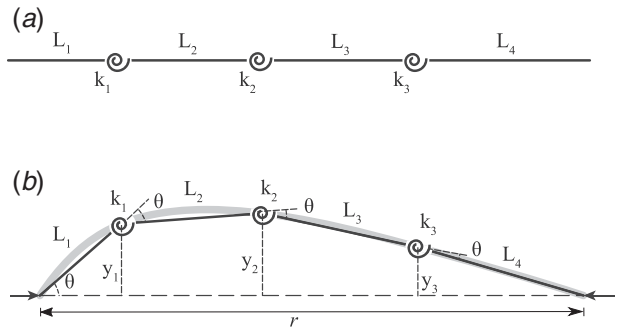

Fig. 2 Rigid-link and torsion spring model showing (*a*) a flat position and (*b*) an actuated position for a rigid-link system of $N = 3$

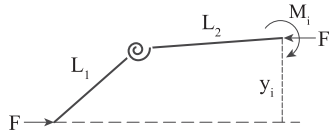

Fig. 3 Free-body diagram of the structure cut at the *i*th joint

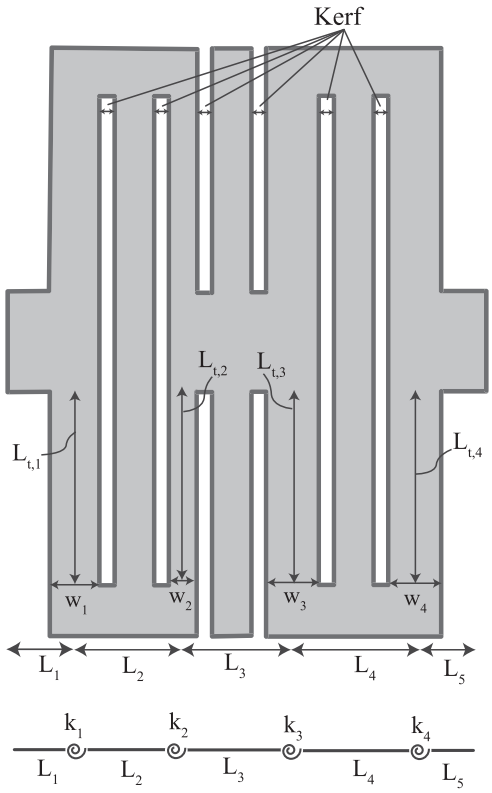

Fig. 4 A chain of LET joints with important dimensions shown with the corresponding model schematic. This chain has five rigid links and four torsion springs.

Chen and Howell developed expressions for the stiffness of a rectangular torsion bar, the basic torsional element of the LET joint, that are symmetric (t and w are interchangeable) [40]. This is helpful for design situations where the geometry is not known a priori. The stiffness expression of a single rectangular bar is repeated here for reference [40]:

$$k = \frac{GJ}{L_t} \tag{4}$$

where G is the shear modulus of the material, L_t is the length of the torsion bar, and in terms of the width w and thickness of the torsion bar t

$$J = \left(\frac{2t^3w^3}{7t^2 + 7w^2}\right)\left(\frac{1.17t^2 + 2.191tw + 1.17w^2}{t^2 + 2.609tw + w^2}\right) \tag{5}$$

The second grouped term in the expression for J can be replaced by a fifth degree polynomial divided by another fifth degree polynomial for greater accuracy (see Ref. [40]) and this more accurate form of the equation was used in the implementation sections of this paper. These terms come from curve fits applied to a compensation function that seeks to resolve the exact series solution with a symmetric approximate solution for the torsional stiffness of a rectangular bar.

Because the value for the stiffness can be determined from the desired geometry with Eq. (3), this can be set equal to the expression for the stiffness of the torsion bar from Eqs. (4) and (5). Moreover, the expression from Eq. (4) is multiplied by a factor m which corresponds to the number of parallel torsion bars along the ruling line of the torsional spring k_i. Rearranging to move all terms to a single side results for joint i

$$0 = \frac{Fy_i}{\theta_i} - \frac{mGJ}{L_t} \tag{6}$$

There is some flexibility in determining which geometric parameter(s) are allowed to vary to satisfy this equation. For example, all terms could be defined except for w and the equation can be solved numerically to find the width of the torsion bar.

For more complex joint types or considering degrees-of-freedom other than just twisting about a single axis, more in-depth stiffness modeling techniques could be used to obtain a relationship between the geometry, loading, and the stiffness [41].

2.2 Joint Placement Optimization. Multidimensional optimization can be used to determine joint locations for a specified number of torsion joints, N, which will minimize the error in approximating the desired profile with a series of rigid links and allow for the introduction of additional constraints in the design problem.

The distances between joint locations, δ_i, are the design variables where $i = 1$ to N. To simplify the optimization, problem constraints are added such that the design variables must be positive and are represented as

$$\delta_i > 0 \tag{7}$$

These constraints ensure that the ordering of the torsion bars does not change through the optimization process. The design variables, δ_i, can be related to d_i and the distances of the torsion springs from one end of the deployed surface where $i = 1$ to N as shown in Fig. 5.

The objective function for the optimization problem can be defined as a minimization of the *areal profile error*, the area between the desired directrix $y_{\text{desired}}(x)$ and the actual deployed shape's directrix $y_{\text{poly}}(x)$ where the subscript *poly* stands for polyline or polygonal chain. The objective function to be minimized is thus written as

$$F(\delta) = \text{Areal profile error} = \int_0^L \left(y_{\text{desired}}(x) - y_{\text{poly}}(x)\right)dx \tag{8}$$

where $y_{\text{poly}}(x)$ is determined from the vector of design variables, δ_i, to create a piecewise function of straight lines representing the rigid links. During implementation, numerical integration was used to evaluate the areal profile error.

It is best to pair this objective function with a constraint on the maximum deviation of the system from the desired curve, the *lineal profile error*. The lineal profile error can be expressed as

$$\begin{aligned}&\text{Lineal profile error}\\ &\quad = \max\left(\text{shortest distance from } y_{\text{desired}}(x_{\text{arb}}) \text{ to } y_{\text{poly}}\right)\end{aligned} \tag{9}$$

where x_{arb} represents an arbitrary point along the desired curve. The constraint on this error's maximum allowable value is defined as

$$\text{Lineal profile error} \leq \begin{matrix}\text{Allowable lineal}\\ \text{Profile error}\end{matrix} \tag{10}$$

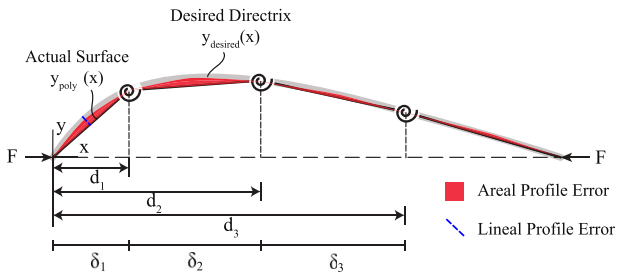

Fig. 5 The design variables, δ_i, are the distances between torsional springs (three shown here). The objective to be minimized, the areal profile error between the desired and actual surface, is shown as the shaded region. The lineal profile error which can be limited with a constraint is also shown.

This prevents the shortest distance from an arbitrary point on $y_{desired}$ to y_{poly} from growing too large. If this constraint is not in place, the optimization process tends to aggregate all of the areal profile error to the location where the curvature of the desired function is the greatest, even if the distance from the desired curve to the actual deployed surface becomes large.

By imposing a limit on the maximum lineal profile error, the minimum areal profile error is increased, but distributed more evenly throughout the system. To gain an appropriate understanding of the range of this constraint, the optimization can be performed with a large value for the allowable lineal profile error such that the constraint is not binding. The value of the constraint can then be reduced until it reaches the other extreme value which will cause the optimization problem to have no feasible solution.

In the implementation to evaluate this constraint, the lineal profile error was found by locating the largest lineal profile error for each segment described by δ_i. This was accomplished with another optimization routine where a single free variable, the x coordinate on $y_{desired}(x)$, was determined to maximize the objective function of the distance between the point $(x, y_{desired}(x))$ and the line segment (found using a form of the distance formula for the shortest length between a point and a line).

In addition to the lineal profile error constraint, to maintain a feasible geometry another constraint should limit the sum of the design variables to a value smaller than the maximum value of x for $y_{desired}$, that is

$$\sum_{i=1}^{N} \delta_i \leq x_{max} \tag{11}$$

If desired, additional constraints can also be introduced such as the maximum angular rotation of a torsional spring and the minimum or maximum lengths of the rigid links. Once a mechanism, such as a torsion bar, is decided upon to serve as the torsion spring, further constraints can be imposed to limit stress or size of the mechanism.

To illustrate these additional constraints, consider a rigid-link system which uses N torsion springs, which corresponds to the number of design variables. Let us assume a geometry similar to the one shown in Fig. 4, where the number of torsion bars on each ruling line is two ($m=2$) and the only geometric parameter we are allowing to change is the torsion bar widths w_i.

Several constraints can be added to ensure functionality and the ability to be manufactured for the torsional joint system. Constraints can be added to require each torsion bar width, w_i, to be greater than or equal to a minimum feasible width, $w_{min,allow}$, represented as

$$w_{min,allow} \leq w_i \quad \text{for} \quad i = 1 \ldots N \tag{12}$$

Constraints can be added to ensure the widths of the torsion bars of the torsion joints, w_i, fit into the dimensions for the link lengths, L_i, while accounting for the kerf from constructing the torsion joints. These constraints can be expressed as

$$\begin{aligned} &\frac{w_1}{2} + \frac{kerf}{2} - L_1 \leq 0 \\ &\frac{w_{i-1}}{2} + \frac{w_i}{2} + kerf - L_i \leq 0 \quad \text{for} \quad i = 2 \ldots N \\ &\frac{w_N}{2} + \frac{kerf}{2} - L_{N+1} \leq 0 \end{aligned} \tag{13}$$

The highest stress in any torsional bar with a displacement angle, θ_i, is a shear stress occurring in middle of the widest side of the torsion bar when stress concentrations are ignored. The highest shear stresses in each torsional bar, τ_i, can be constrained to be less than an allowable shear stress value, τ_{allow}:

$$\tau_i \leq \tau_{allow} \tag{14}$$

To calculate the highest shear stresses in each torsion bar, a symmetric formula has been developed and can be used where t and w are once again interchangeable [42] as

$$\tau_i = \frac{2.4M_i(w+t)}{w^2t^2}\left(\frac{1.271v^2 + 0.2829v + 0.0498}{v^2 + 0.27v + 0.0496}\right) \tag{15}$$

where $v = |\log t/w|$. Similar to Eq. (5), a more accurate, higher order term resulting from curve fits is available for the second grouped term (see Ref. [42] for details) and this more accurate term was used in the implementation sections of this paper.

Scaling of the desired profile and constraints was used to increase the convergence rate for the optimization during implementation. For example, the desired profile and allowable lineal profile error were scaled by a factor such that the maximum x-axis length of the desired profile was one, though care was taken to use the full-scale geometry when calculating dimensions such as widths, stresses, or the constraints in Eq. (13). Several constraints, such as Eqs. (10), (12), and (14), were scaled by their allowable values.

2.2.1 Joint Placemsent for Parabolic Profiles. During the implementation of the optimization algorithm for parabolic profiles, it was noted that when the additional constraints for lineal profile error, stress, and manufacturing were not binding, the minimum areal profile error was achieved through equal δ_i spacing of the torsion springs. This can be shown mathematically as follows.

PROPOSITION 1. *Let $f(x)$ be a function whose graph is a parabola on the interval $[\alpha, \beta]$.* Let *P be the polyline consisting of n line segments with endpoints, $(x_0 = \alpha, f(x_0))$, $(x_1, f(x_1))$, $(x_2, f(x_2)), \ldots, (x_{n-1}, f(x_{n-1}))$, $(x_n = \beta, f(x_n))$. If P minimizes the areal profile error between itself and the parabola, then $x_{i+1} - x_i = ((\beta - \alpha)/n)$ for $i = 0, 1, \ldots, n-1$; i.e., the points are equally spaced along the x-axis.*

Proof. Without loss of generality, we suppose that $\alpha = 0$ and that the parabola is above the x-axis on the interval $[0, \beta]$. The function $f(x)$ can be written as $f(x) = ax^2 + bx + c$ for some real numbers a, b, and c. We give a proof by induction on n.

If $n = 2$, then P consists of the points $(0, f(0))$, $(x_1, f(x_1))$, and $(\beta, f(\beta))$. Let T_1 denote the trapezoid formed from the points $(0, 0)$, $(0, f(0))$, $(x_1, f(x_1))$, and $(x_1, 0)$. Let T_2 denote the trapezoid formed from the points $(x_1, 0)$, $(x_1, f(x_1))$, $(\beta, f(\beta))$, and $(\beta, 0)$. Let $A(T_1)$ and $A(T_2)$ denote the areas of the two trapezoids, respectively. The sum of these two areas can be expressed as function of x_1 as follows:

$$\begin{aligned} A(T_1) + A(T_2) &= \frac{1}{2}(f(0) + f(x_1))x_1 \\ &\quad + \frac{1}{2}(f(x_1) + f(\beta))(\beta - x_1) \\ &= \frac{1}{2}(c + ax_1^2 + bx_1 + c)x_1 \\ &\quad + \frac{1}{2}(ax_1^2 + bx_1 + c + a\beta^2 + b\beta + c)(\beta - x_1) \\ &= \frac{1}{2}(cx_1 + ax_1^3 + bx_1^2 + cx_1 + \beta ax_1^2 + \beta bx_1 \\ &\quad + \beta c + a\beta^3 + b\beta^2 + c\beta \\ &\quad - ax_1^3 - bx_1^2 - cx_1 - a\beta^2 x_1 - b\beta x_1 - cx_1) \\ &= \frac{1}{2}(\beta ax_1^2 - \beta^2 ax_1 + \beta c + \beta^3 a + \beta^2 b + \beta c) \end{aligned}$$

To maximize or minimize this function, we take a derivative with respect to x_1 which results in $(1/2)(2\beta a\, x_1 - \beta^2\, a)$. Setting this equal to 0 gives $x_1 = \beta/2$. The second derivative of the function is βa. Recall $\beta > 0$. Thus if a is negative, then the area function above is concave down and thus the function is maximized at $x_1 = \beta/2$. When a is negative, the parabola given by $f(x)$ is also concave down. Thus, in this case, maximizing $A(T_1) + A(T_2)$ is equivalent

to minimizing the areal profile error between P and the parabola. If a is positive, then the second derivative of the area function is positive and thus the area function is minimized at $x_1 = \beta/2$. In this case, the parabola is concave up and minimizing $A(T_1) + A(T_2)$ is equivalent to minimizing the areal profile error between P and the parabola. Therefore, in either case, the areal profile error between the parabola and P is minimized when x_1 is placed half way between a and b. This completes the base case.

Suppose the result holds when $n = 1, 2, 3, \ldots, k$ for some integer k. Let P be a polyline consisting of $k+1$ line segments that minimizes the areal profile error. Consider the first k line segments. The x coordinates of the endpoints are $0, x_1, x_2, \ldots, x_k$. Note that the polyline consisting of these k line segments, call it P_k, must minimize the area profile error between P_k and the parabola given by $f(x)$ on the interval $[\alpha, x_k]$. This is because if P_k did not minimize the areal profile error, then taking a polyline that did minimize this error and attaching the $k+1$ line segment from P would produce a polyline with a smaller areal profile error than P, a contradiction. Thus by the inductive hypothesis, $0, x_1, x_2, \ldots, x_k$ are equally spaced along the x-axis.

Now consider the last two line segments of P, line segments k and $k+1$. The x coordinates of the endpoints are x_{k-1}, x_k and $x_{k+1} = \beta$. By a similar argument as above, the polyline consisting of these line segments minimizes the areal profile error between itself and the parabola given by $f(x)$ on the interval $[x_{k-1}, \beta]$. Thus by the inductive hypothesis, x_{k-1}, x_k, and β are equally spaced along the x-axis.

Since the numbers in the overlapping lists $(0, x_1, x_2, \ldots, x_k)$ and (x_{k-1}, x_k, β) are equally spaced, the numbers in the list $(x_0, x_1, x_2, \ldots, x_k, \beta)$ are equally spaced. Therefore, $x_{i+1} - x_i = (\beta - \alpha)/(k+1)$ for $i = 0, 1, 2, 3, \ldots, k$. This completes the inductive step and thus the result holds for all positive integers n. ∎

2.3 Shape Throughout Deployment. The shape the surface takes throughout deployment as a function of the deployment force can be determined once joint placements have been selected and the stiffness of each joint calculated that is required for the desired profile and deployment force. That is, we assume k_i and L_i are known for each joint from $i = 1$ to N, and we want to solve for the force–displacement behavior where F is the actuation force with corresponding angles θ_i, where $i = 0$ to N to fully define the position of the surface. A system of equations governing the shape's force–displacement behavior is setup in the following way. A constraint is established by summing the vectors representing the links from Fig. 2(*b*) about a loop where the horizontal components are

$$L_1 \cos\theta_0 + \sum_{i=1}^{N}\left(L_{i+1}\cos\left(\theta_0 - \sum_{j=1}^{i}\theta_j\right)\right) - r = 0 \tag{16}$$

where r is the distance between the actuation forces and the vertical components

$$L_1 \sin\theta_0 + \sum_{i=1}^{N}\left(L_{i+1}\sin\left(\theta_0 - \sum_{j=1}^{i}\theta_j\right)\right) = 0 \tag{17}$$

Using the free-body diagram from Fig. 3, N additional equations can be written, where the moment–balance relationship for the first joint k_1 is

$$F(L_1 \sin\theta_0) = k_1\theta_1 \tag{18}$$

and for the remaining joints for $q = 2$ to N as

$$F\left[L_1 \sin\theta_0 + \sum_{i=1}^{q-1}\left(L_{i+1}\sin\left(\theta_0 - \sum_{j=1}^{i}\theta_j\right)\right)\right] = k_q\theta_q \tag{19}$$

Equations (17), (18), and (19) give $N+1$ equations which can be solved for the $N+1$ angles of θ_i, where $i = 0$ to N when subjected to a force F. Equation (16) can then be used to find the distance between r between the ends of the deployable surface.

This system of equations is amenable to solving numerically with a single unknown and using substitutions. Let θ_0 be a single unknown and use Eq. (18) to calculate θ_1. The process can then be continued to sequentially calculate each θ_q for $q = 2$ to N using Eq. (19). These values can then be used in Eq. (17) as the single equation to satisfy.

This set of equations can have multiple valid solutions corresponding to stable and unstable equilibrium configurations of the deployable surface. The stable configurations correspond with minimums in the potential energy of the system. Kinematic chains with passive joints with stiffness can have multiple equilibrium positions as demonstrated in Ref. [8]. For the deployable surfaces in this research, an additional stable position is observed by reflecting a convex deployable surface about the line of action of the actuation force. Unstable equilibrium positions can be observed when links create a zig-zag shape, where some joint angles are positive and others are negative. Limiting the domain of the joint angles and providing an initial guess to the solver of a convex profile can help ensure that the system of equations is solved for a stable equilibrium position where a convex profile is formed. In-depth characterization of all equilibrium states is left to future work.

3 Results

The methodology described above was used to create prototypes of a deployable airfoil surface and deployable parabolic reflector.

3.1 Deployable Airfoil Surface. A deployable airfoil surface was designed using torsion bars as the torsion springs in the model with optimization to place the joint locations and ensure constraints for the lineal profile error and for manufacturing were met. The desired directrix was chosen to be the top surface of a Clark Y airfoil with a 10 in. (25.4 cm) chord length [43]. The optimization and constraint setup parameters are reported in Table 1.

The resulting joint positions after the optimization are shown by the thick black line in Fig. 6(*a*). The stiffnesses required for the desired profile and actuation force were calculated and the corresponding LET joint geometry determined. With the stiffness values for the joints, the shape throughout deployment was calculated as described in Sec. 2.3 and plotted in Fig. 6(*a*). The force-deployment shape results were used to plot the maximum height of the deployed shape against the deployment force as shown in Fig. 6(*b*). This plot shows how small amounts of shape change occur as the actuation force increases until a critical buckling force where large amounts of deformation occur rapidly. This nonlinear shift in stiffness has been investigated for kinematic chains containing joints with passive stiffness [8].

The resulting LET joint pattern was cut from a polypropylene sheet using an abrasive waterjet. The pattern is shown in the flat and deployed states in Fig. 7. The optimization results and

Table 1 Optimization parameters for a deployable airfoil surface made from polypropylene

Parameter	Value
Number of torsion springs (N)	12
Tip load force (F)	0.5 lb (2.22 N)
Shear modulus (G)	64.4 ksi (444 MPa)
Thickness of panel (t)	0.063 in. (1.60 mm)
L_t	1.3 in. (3.3 cm)
m	2
$w_{\min,\text{allow}}$	0.06 in. (1.5 mm)
kerf	1/16 in. (1.59 mm)
τ_{allow}	1590 psi (11.0 MPa)
Allowable lineal profile error	0.04 in. (1.0 mm)

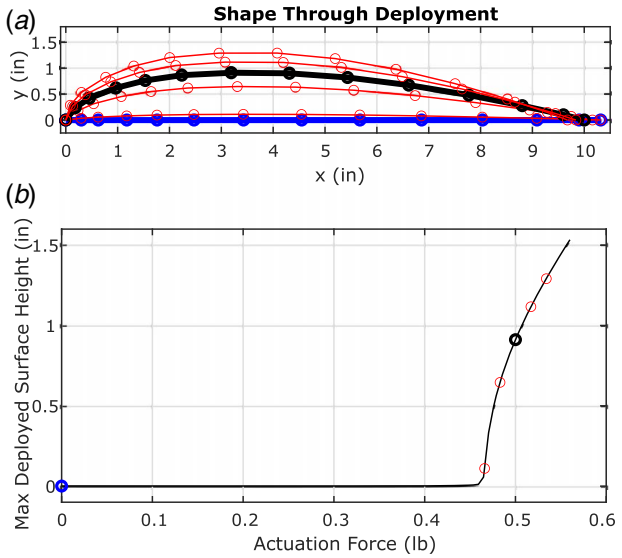

Fig. 6 (*a*) The optimized joint locations on the desired airfoil profile shown by the points on the thick black line while the thin red lines show the shape for actuation tip loads up to and beyond deployment to the desired profile. The thick blue line represents the flat, undeployed surface. (*b*) The maximum height of the deployed shape versus the actuation force with points corresponding to the profiles is shown in part (*a*). (Color version online.)

experimental measurements taken on the prototype are summarized in Table 2. Basic photogrammetry was carried out using MATLAB to measure approximate lineal profile error in the deployed shape. The largest error occurred in the leading edge where some parasitic or unwanted motion occurred due to compression of the LET joints by the tip loads. A thin polyethylene terephthalate (PET) adhesive film 2.5 mils (0.064 mm) thick was then applied to the top layer of the pattern to decrease the parasitic motion while minimally affecting the torsion performance, similar to a technique

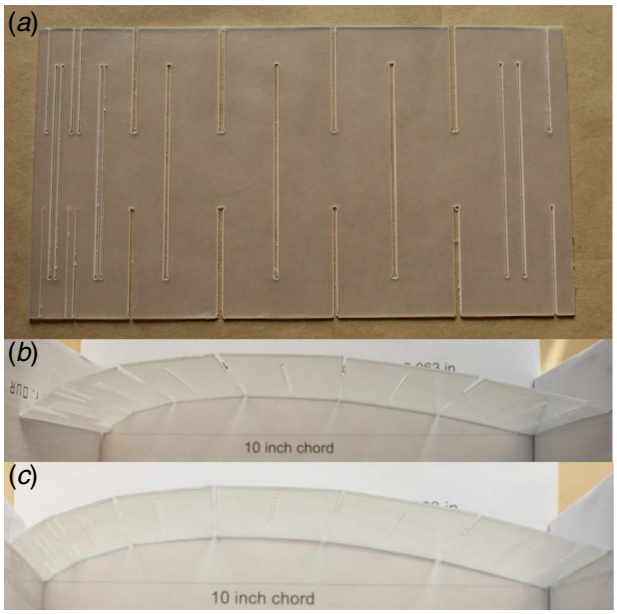

Fig. 7 Deployable top surface of a Clark Y airfoil made from polypropylene using an abrasive water jet, where (*a*) is the flat surface, (*b*) is the deployed surface, and (*c*) is the deployed surface with a PET membrane to reduce parasitic motion

Table 2 Optimization and experimental results for a deployable airfoil surface made of polypropylene

Parameters	Min value	Max value
Deployed spacing, δ_i	0.181 in. (4.60 mm)	1.142 in. (29.0 mm)
Link lengths, L_i	0.298 in. (7.57 mm)	1.155 in. (29.3 mm)
Widths, w_i	0.084 in. (2.13 mm)	1.081 in. (27.5 mm)
w_i/t ratios	1.33	17.16
Parameters from optimization results		**Value**
Lineal profile error		0.023 in. (0.584 mm)
Areal profile error		0.046 in.^{2} (0.30 cm^2)
τ_{max}		795 psi (5.48 MPa)
Shear stress factor of safety		2.004
Undeployed (flat) length		10.315 in. (26.2 cm)
Experimentally measured values		**Value**
Lineal profile error (photogrammetry)		
Without PET covering		≈0.036 in. (0.914 mm)
With PET covering		≈0.057 in. (1.45 mm)
Force to deploy to profile (from scale)		0.35 ± 0.1 lb
		(1.56 ± 0.44 N)

investigated by Chen et al. [44]. This appeared to reduce some of the parasitic motion, yet increased the lineal profile error. The pattern with the PET covering is shown in Fig. 7(*c*). Applying a thin film with full bonded contact along a surface can impact the neutral axis of bending and torsional axes and thus change the modeling, and some options exist to minimize this impact. Specifically, a sandwich structure where the thin film is applied between two sheets of the same thickness can maintain the neutral axis of bending and torsional axes locations. Another option is to adhere the film to only the areas of the pattern that are not in torsion to help maintain the torsional behavior of the joints, as is further discussed in Ref. [44].

The force to deploy the pattern to the profile was measured using a small digital scale. Accurate, repeatable measurements were limited with the current measurement setup and more rigorous instrumentation is recommended for future work. There is some discrepancy between the designed tip load force and the measured force. This could be due to a number of factors including errors in the shear modulus value used, manufactured kerf width, and perhaps most importantly bending observed from compressive forces in the structure that accompanied the torsional deflection.

3.2 Deployable Parabolic Reflector. The model was also used to design a deployable parabolic reflector made of Aluminum 7075-T6. The target deployed shape has a focal point 4 in. from the vertex. The flat, undeployed dimensions are 18.36 × 10.2 in. (46.6 × 25.9 cm). The parameters used to setup the optimization are shown in Table 3. The optimized joint locations are shown on the thick black line in Fig. 8(*a*). As was done with the airfoil from the previous section, the calculated stiffnesses of the joints were used with the procedure in Sec. 2.3 to trace the shape through deployment and beyond the desired deployment shape as shown by the red profiles in Fig. 8(*a*). The tip load force was plotted against the maximum deployed surface height in Fig. 8(*b*) with points shown corresponding to the profiles plotted in part (*a*) of the figure. The presence of a critical load that results in buckling-like behavior is present in the plot.

The optimized parabolic reflector was manufactured from the aluminum using an abrasive water jet and is shown in the flat and deployed states in Fig. 9. The same testing setup as for the airfoil surface was used to experimentally determine a force at the

Table 3 Optimization parameters for a deployable parabolic surface made of aluminum

Parameter	Value
Number of torsion springs (N)	22
Tip load force (F)	1.75 lb (7.78 N)
Shear modulus (G)	3,910 ksi (26.96 GPa)
Thickness of panel (t)	0.040 in. (1.0 mm)
L_t	0.9 in. (2.29 cm)
m	6
$w_{\text{min,allow}}$	0.1 in. (2.54 mm)
$kerf$	1/16 in. (1.59 mm)
τ_{allow}	38,800 psi (268 MPa)
Allowable lineal profile error	0.060 in. (1.52 mm)

desired deployed profile and photogrammetry was used to investigate the error in the profile. The resulting values of the final geometry and from experimental testing are described in Table 4. The deployed profile and desired profile matched quite well with a small observed lineal profile error. The required tip load force to achieve the desired profile also matched with small error. Considerably less bending was seen in this prototype than for the airfoil surface and no covering was used.

4 Discussion

Certain tradeoffs from employing torsion bars to create deployable surfaces can be illuminated by rearranging Eq. (6) as

$$(F)\left(\frac{1}{G}\right)\left(\frac{y_i}{\theta_i}\right) = \left(\frac{mJ}{L_t}\right) \tag{20}$$

From left to right, these terms are determined by the desired actuation force, the material used, and the desired profile curve, and on

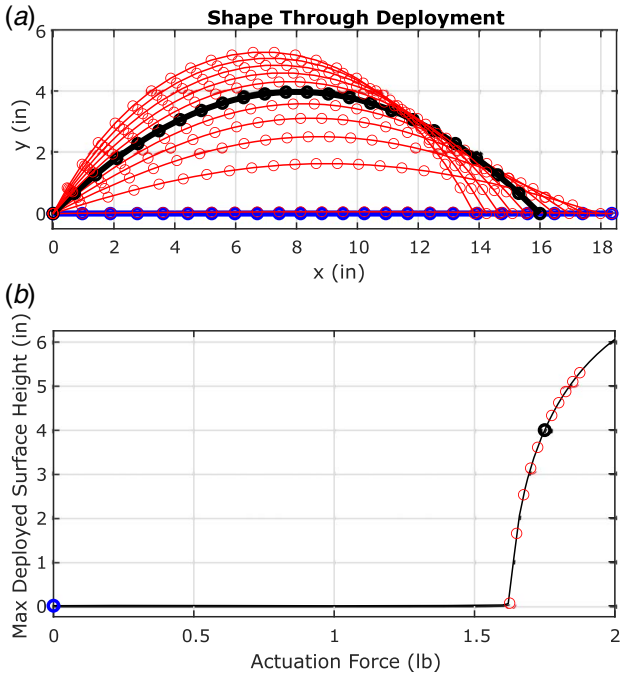

Fig. 8 (*a*) The optimized joint locations on the desired parabolic profile are shown by the points on the thick black line while the thin red lines show the shape for actuation tip loads up to and even beyond deployment to the desired profile. The thick blue line represents the flat, undeployed surface. (*b*) The maximum height of the deployed shape versus the actuation force with points corresponding to the profiles is shown in part (*a*). (Color version online.)

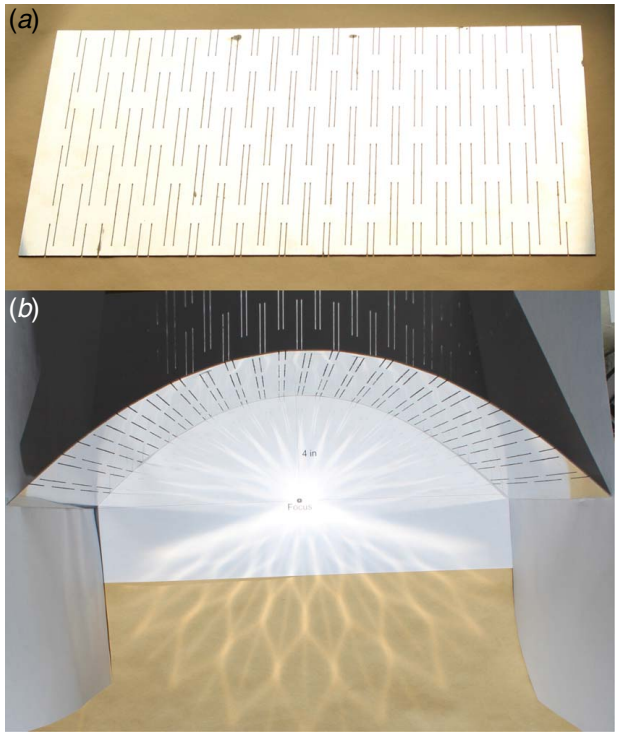

Fig. 9 Deployable parabolic reflector made of aluminum, where (*a*) is the flat state and (*b*) is the deployed state with light reflecting off the surface

the right side of the equation all the factors in the term are functions of the geometry of the torsion bar pattern. By grouping these terms, we can see relationships such as if the geometry of a pattern is maintained (the right side of the equation), and changing the material will scale the actuation force as long as the stresses do not exceed the new material's stress limit. Similarly, errors in estimating the value used for the shear modulus of a material should not affect the ability to achieve a desired profile shape as long as one is willing to adjust the actuation force to compensate for the modulus error.

It is also informative to look at an expression for the angular deflection of a torsion bar in terms of shear stress. Since a prescribed profile results in a displacement-limited design, rather than torque-limited design, the maximum stress in the system can be lessened by requiring smaller angular deflections and reducing the stiffness.

Table 4 Optimization and experimental results for a deployable parabolic surface from aluminum

Parameters	Min value	Max value
Deployed spacing, δ_i	0.696 in. (17.7 mm)	0.696 in. (17.7 mm)
Link lengths, L_i	0.696 in. (17.7 mm)	0.963 in. (24.5 mm)
Widths, w_i	0.158 in. (4.0 mm)	0.460 in. (11.7 mm)
w_i/t ratios	3.94	11.49
Parameters from optimization results		**Value**
Lineal profile error		0.008 in. (0.20 mm)
Areal profile error		0.081 in.^{2} (0.52 cm^2)
$\tau_{\max}$		15.1 kpsi (104 MPa)
Shear stress factor of safety		2.57
Undeployed (flat) length		18.361 in. (46.6 cm)
Experimentally measured values		**Value**
Lineal profile error (photogrammetry)		≈0.018 in.(0.46 mm)
Force to deploy to profile (from load cell)		1.8 ± 0.1 lb (8.0 ± 0.44 N)

Using Eqs. (1), (4), (5), and (15), we can write the angular deflection for a torsion bar as

$$\theta_i = \frac{\tau_i L_t}{G} f(t, w) \tag{21}$$

where $f(t, w)$ is a function of t and w that depends on which form of J in Eq. (15) is selected (the higher order more accurate expression or expression presented in the equation). From this form, we can see that there are several options to achieve the required deflections. The first is to reduce the required deflections θ_i themselves. This can be accomplished by increasing the number of torsion joints N which in turn lowers the θ_i magnitudes. The maximum number of joints N that can be introduced reaches a limit imposed by the manufacturing constraints that the widths of the torsion bars must fit within the link lengths. A second option to achieve required deflections is to choose a material with a high ratio of maximum shear stress to shear modulus. Several materials and these ratios are shown in Table 5 to provide a comparison of how amenable a material is to large deflection of torsion bars with values coming from supplier material data sheets and Ref. [45]. The third option to obtain the required deflections is to increase the torsion bar lengths, L_t. This can be limited by space constraints and also the introduction of unacceptable parasitic motions other than torsion when the torsion bar lengths are extended. Finally, t and w can be selected such that $f(t, w)$ results in as large as values as possible. Chen and Howell recommend a ratio of t/w to be ≤ 0.35, $=1$, or ≥ 2.86 to accomplish this [42].

Equation (20) implies that the number of torsion bars along a ruling line m can be changed to affect the magnitude of the tip load, yet m has no effect upon the stress, as m is not present and does not affect any of the terms in Eq. (21).

Minimizing the areal profile error in the model pushed all of the error between the desired and deployed directrix to the area of greatest curvature of the desired directrix. This was corrected by placing a constraint on the lineal profile error. The effect of minimizing the lineal profile error with a constraint on the areal profile error was also investigated with similar results, though the optimizer required more iterations to converge. Further investigation of definitions of profile error and suitable objective functions to minimize the error for the model present possible directions for future work.

As seen in the results from the physical prototypes, it appeared that bending accompanied the torsional deflection. Work can be done to incorporate bending effects into the analytical modeling for more accurate design estimates.

Both prototypes were deployed by moving two smooth barriers towards one another to create a compressive force. Tension elements, such as cables or strings, could be used to pull the two edges of the panel together to create an ultra-lightweight actuation method, though the effects of the point loads caused from the elements should be considered.

Table 5 A small sample of possible materials for torsion bars

Material	$1000 \times \tau_{yield}/G$
Polymethyl methacrylate (PMMA)	24.5[a]
Polypropylene	24
Titanium (Ti–6Al–4V)	11.7
Steel (4340)	11
Aluminum (7075-T6)	9.9

Note: Materials with high ratios of shear yield stress, τ_{yield}, to shear modulus, G, are good candidates for maximizing deflection in deflection-limited torsion bar geometries (property values from supplier data sheets and Ref. [45], with approximations as required for shear modulus by $G = E/(2(1+\nu))$ and shear yield strength $\tau_{yield} \approx 0.577\sigma_{yield}$, where σ_{yield} is the tensile yield strength).

[a]While PMMA has an excellent ratio, it is a brittle material and susceptible to stress concentrations.

The model constructed using chains of torsion joints results in a deployable surface that can function as the final surface or as a structure underneath a flexible skin. Further studies need to be conducted to see how well the deployed surface would behave if used in an application with multiple loading conditions, such as with a distributed pressure load from an aerodynamic loading. Because aerodynamic loads fluctuate, it poses a challenge to design a single structure for multiple load cases where both the deployed structure's stability and aerodynamic stability are considered. One possible path forward to address a more complex loading scenario would be to use a support structure underneath the deployed surface where hard stops align during deployment to resist compression loads on the surface of the structure.

5 Conclusion

A model has been presented as a way to create generalized cylindrical deployable surfaces with convex directrices conducive to being implemented with torsional compliant joints. The shape during the deployment process is also described. The model is demonstrated using the torsion bars of LET joints as torsion springs. A multidimensional optimization model was used to efficiently locate a given number of compliant joints along the directrix to minimize the error between the desired and actual directrix. Constraints were also enforced to ensure performance and a manufacturable geometry. The model was demonstrated through the physical creation of several prototypes in various materials. While the methodology shows potential for advancing the design of precise deployable surfaces, further investigation of the effects of bending accompanying the torsion and the effects of various loading conditions upon the deployed surfaces should be conducted. Actuation methods could also be incorporated into the material itself to create a compact package that can morph when a stimulus is applied.

Acknowledgment

This material is based on work supported by the National Science Foundation under NSF Grant 1663345 and NSF GRFP Grant 1247046. The authors acknowledge the University of Southern Indiana (USI) Foundation for supporting this research through a Science, Engineering, and Education Research Grant Award (SEERGA) and Justin Amos for his assistance with prototype fabrication. The authors would also like to acknowledge John Sinkovic for his insight into proving the optimal spacing for parabolic profiles where additional constraints were not binding.

Conflict of Interest

There are no conflicts of interest.

Data Availability Statement

The authors attest that all data for this study are included in the paper. Data provided by a third party are listed in Acknowledgement.

References

[1] Nelson, T. G., Baldelomar Pinto, L. M., Bruton, J. T., Deng, Z., Nelson, C. G., and Howell, L. L., 2020, "Deployable Convex Generalized Cylindrical Surfaces Using Torsional Joints," ASME 2020 IDETC/CIE, Virtual, Online, Aug. 17–19.

[2] Struik, D. J., 1961, *Lectures on Classical Differential Geometry*, 2nd ed., Addison-Wesley, Reading, MA.

[3] Cammarata, A., 2016, "Unified Formulation for the Stiffness Analysis of Spatial Mechanisms," Mech. Mach. Theory, **105**(11), pp. 272–284.

[4] Klimchik, A., Pashkevich, A., and Chablat, D., 2019, "Fundamentals of Manipulator Stiffness Modeling Using Matrix Structural Analysis," Mech. Mach. Theory, **133**(3), pp. 365–394.

[5] Pozzi, M., Miguel, E., Deimel, R., Malvezzi, M., Bickel, B., Brock, O., and Prattichizzo, D., 2018, "Efficient FEM-Based Simulation of Soft Robots Modeled as Kinematic Chains," 2018 IEEE International Conference on Robotics and Automation (ICRA), Brisbane, Australia, May 21–25, pp. 4206–4213.
[6] Klimchik, A., Pashkevich, A., and Chablat, D., 2013, "CAD-Based Approach for Identification of Elasto-Static Parameters of Robotic Manipulators," Finite Elements Anal. Des., **75**(12), pp. 19–30.
[7] Gosselin, C., 1990, "Stiffness Mapping for Parallel Manipulators," IEEE Trans. Rob. Autom., **6**(3), pp. 377–382.
[8] Pashkevich, A., Klimchik, A., and Chablat, D., 2011, "Enhanced Stiffness Modeling of Manipulators With Passive Joints," Mech. Mach. Theory, **46**(5), pp. 662–679.
[9] Majou, F., Gosselin, C., Wenger, P., and Chablat, D., 2007, "Parametric Stiffness Analysis of the Orthoglide," Mech. Mach. Theory, **42**(3), pp. 296–311.
[10] Chillara, V., and Dapino, M. J., 2020, "Review of Morphing Laminated Composites," ASME Appl. Mech. Rev., **72**(1), p. 010801.
[11] Aoki, M., and Juang, J.-Y., 2018, "Forming Three-Dimensional Closed Shapes From Two-Dimensional Soft Ribbons by Controlled Buckling," R. Soc. Open Sci., **5**(2), p. 171962.
[12] Shaw, L. A., and Hopkins, J. B., 2016, "An Actively Controlled Shape-Morphing Compliant Microarchitectured Material," ASME J. Mech. Rob., **8**(2), p. 021019.
[13] Kotikian, A., McMahan, C., Davidson, E. C., Muhammad, J. M., Weeks, R. D., Daraio, C., and Lewis, J. A., 2019, "Untethered Soft Robotic Matter With Passive Control of Shape Morphing and Propulsion," Sci. Rob., **4**(33), p. 7044.
[14] Alfattani, R., and Lusk, C., 2020, "Shape-Morphing Using Bistable Triangles With Dwell-Enhanced Stability," ASME J. Mech. Rob., **12**(5), p. 051003.
[15] Faber, J. A., Arrieta, A. F., and Studart, A. R., 2018, "Bioinspired Spring Origami," Science, **359**(6382), pp. 1386–1391.
[16] Lee, D.-Y., Jung, G.-P., Sin, M.-K., Ahn, S.-H., and Cho, K.-J., 2013, "Deformable Wheel Robot Based on Origami Structure," 2013 IEEE International Conference on Robotics and Automation (ICRA), Karlsruhe, Germany, May 6–10, IEEE, pp. 5612–5617.
[17] Kuribayashi, K., Tsuchiya, K., You, Z., Tomus, D., Umemoto, M., Ito, T., and Sasaki, M., 2006, "Self-Deployable Origami Stent Grafts as a Biomedical Application of Ni-Rich TiNi Shape Memory Alloy Foil," Mater. Sci. Eng. A, **419**(1), pp. 131–137.
[18] Peraza Hernandez, E. A., Hartl, D. J., Malak, R. J., Akleman, E., Gonen, O., and Kung, H. -W., 2016, "Design Tools for Patterned Self-Folding Reconfigurable Structures Based on Programmable Active Laminates," ASME J. Mech. Rob., **8**(3), p. 031015.
[19] Liu, L., Qiao, C., An, H., and Pasini, D., 2019, "Encoding Kirigami Bi-materials to Morph on Target in Response to Temperature," Sci. Rep., **9**(1), pp. 1–14.
[20] Cheng, Y.-C., Lu, H.-C., Lee, X., Zeng, H., and Priimagi, A., 2020, "Kirigami-Based Light-Induced Shape-Morphing and Locomotion," Adv. Mater., **32**(7), p. 1906233.
[21] Lentink, D., Müller, U., Stamhuis, E., De Kat, R., Van Gestel, W., Veldhuis, L., Henningsson, P., Hedenström, A., Videler, J. J., and Van Leeuwen, J. L., 2007, "How Swifts Control Their Glide Performance With Morphing Wings," Nature, **446**(7139), pp. 1082–1085.
[22] Vasista, S., Tong, L., and Wong, K., 2012, "Realization of Morphing Wings: A Multidisciplinary Challenge," J. Air, **49**(1), pp. 11–28.
[23] Wang, H. V., and Rosen, D. W., 2006, "An Automated Design Synthesis Method for Compliant Mechanisms With Application to Morphing Wings," ASME 2006 IDETC/CIE, Philadelphia, PA, Sept. 10–13, ASME, pp. 231–239.
[24] Yokozeki, T., Takeda, S.-I., Ogasawara, T., and Ishikawa, T., 2006, "Mechanical Properties of Corrugated Composites for Candidate Materials of Flexible Wing Structures," Compos. Part A: Appl. Sci. Manuf., **37**(10), pp. 1578–1586.
[25] Chen, M., Liu, J., and Skelton, R. E., 2020, "Design and Control of Tensegrity Morphing Airfoils," Mech. Res. Commun., **103**(1), p. 103480.
[26] Thomson, M. W., 1999, "The Astromesh Deployable Reflector," IEEE Antennas and Propagation Society International Symposium, Orlando, FL, July 11–16, Vol. 3, IEEE, pp. 1516–1519.
[27] Stern, I., 2003, "Deployable Reflector Antenna With Tensegrity Support Architecture and Associated Methods," Apr. 1, U.S. Patent 6,542,132.
[28] Tan, L. T., and Pellegrino, S., 2004, "Ultra Thin Deployable Reflector Antennas," Proceedings of the 45th AIAA/ASME/ASCE/AHS/ASC Structures, Structural Dynamics and Materials Conference, Palm Springs, CA, Apr. 19–22.
[29] Kaplan, R., and Schultz, J. L., 1977, "Deployable Reflector Structure," Jun. 14, U.S. Patent 4,030,102.
[30] Freeland, R., Bilyeu, G., and Veal, G., 1995, "Validation of a Unique Concept for a Low-Cost, Lightweight Space-Deployable Antenna Structure," Acta Astronaut., **35**(9), pp. 565–572.
[31] Funke, L. W., and Schmiedeler, J. P., 2017, "Simultaneous Topological and Dimensional Synthesis of Planar Morphing Mechanisms," ASME J. Mech. Rob., **9**(2), p. 021009.
[32] Zhao, K., Schmiedeler, J. P., and Murray, A. P., 2012, "Design of Planar, Shape-Changing Rigid-Body Mechanisms for Morphing Aircraft Wings," ASME J. Mech. Rob., **4**(4), p. 041007.
[33] Nelson, T. G., Lang, R. J., Pehrson, N. A., Magleby, S. P., and Howell, L. L., 2016, "Facilitating Deployable Mechanisms and Structures Via Developable Lamina Emergent Arrays," ASME J. Mech. Rob., **8**(3), p. 031006.
[34] Jacobsen, J. O., Chen, G., Howell, L. L., and Magleby, S. P., 2009, "Lamina Emergent Torsional (LET) Joint," Mech. Mach. Theory, **44**(11), pp. 2098–2109.
[35] Xie, Z., Qiu, L., and Yang, D., 2017, "Design and Analysis of Outside-Deployed Lamina Emergent Joint (OD-LEJ)," Mech. Mach. Theory, **114**(8), pp. 111–124.
[36] Xie, Z., Qiu, L., and Yang, D., 2018, "Design and Analysis of a Variable Stiffness Inside-Deployed Lamina Emergent Joint," Mech. Mach. Theory, **120**(2), pp. 166–177.
[37] Delimont, I. L., Magleby, S. P., and Howell, L. L., 2015, "A Family of Dual-Segment Compliant Joints Suitable for Use as Surrogate Folds," ASME J. Mech. Des., **137**(9), p. 092302.
[38] Nelson, T. G., Bruton, J. T., Rieske, N. E., Walton, M. P., Fullwood, D. T., and Howell, L. L., 2016, "Material Selection Shape Factors for Compliant Arrays in Bending," Mater. Des., **110**(22), pp. 865–877.
[39] Pehrson, N. A., Bilancia, P., Magleby, S. P., and Howell, L. L., 2020, "Load–Displacement Characterization in Three Degrees of Freedom for General LET Arrays," ASME J. Mech. Des., **142**(9), p. 093301.
[40] Chen, G., and Howell, L. L., 2009, "Two General Solutions of Torsional Compliance for Variable Rectangular Cross-Section Hinges in Compliant Mechanisms," Precis. Eng., **33**(3), pp. 268–274.
[41] Quennouelle, C., and Gosselin, C., 2008, "Stiffness Matrix of Compliant Parallel Mechanisms," ASME 2008 IDETC/CIE, Brooklyn, NY, Aug. 3–6, pp. 151–161.
[42] Chen, G.-M., and Howell, L. L., 2018, "Symmetric Equations for Evaluating Maximum Torsion Stress of Rectangular Beams in Compliant Mechanisms," Chin. J. Mech. Eng., **31**(1), p. 14.
[43] Selig, M., 2020, "UIUC Airfoil Data Site," Department of Aerospace Engineering, University of Illinois, https://m-selig.ae.illinois.edu/ads/coord_database.html
[44] Chen, G., Magleby, S. P., and Howell, L. L., 2018, "Membrane-Enhanced Lamina Emergent Torsional Joints for Surrogate Folds," ASME J. Mech. Des., **140**(6), p. 062303.
[45] Callister, W. D., and Rethwisch, D. G., 2018, *Materials Science and Engineering: An Introduction*, Wiley, New York.